Biosensors and Bioelectronics xxx (xxxx) xxx

Contents lists available at ScienceDirect

Biosensors and Bioelectronics

journal homepage: http://www.elsevier.com/locate/bios

Laser-induced noble metal nanoparticle-graphene composites enabled flexible biosensor for pathogen detection

Zhiheng You [a], Qiming Qiu [a], Huayun Chen [a], Yuyan Feng [a], Xiao Wang [a], Yixian Wang [a,*], Yibin Ying [a,b]

[a] School of Biosystems Engineering and Food Science, Zhejiang University, Hangzhou, 310058, PR China
[b] Zhejiang A&F University, Hangzhou, 311300, PR China

ARTICLE INFO

Keywords:
Two-dimensional nanomaterials
Hybrid composites
Laser-induced graphene
Flexible immunosensor
Interdigitated array electrode
Pathogen detection

ABSTRACT

Noble metal nanoparticle-3D graphene hybrid nanocomposites possess the advantage of nanoparticles and graphene, which have attracted extensive interest. Here we developed a one-step laser induction method to prepare various noble metal nanoparticle-3D graphene nanocomposites. The nanocomposites were converted from polyimide film coated with the corresponding metal precursor-chitosan hydrogel ink. These nanoparticles including gold nanoparticles (AuNPs), silver nanoparticles (AgNPs), and platinum nanoparticles (PtNPs), were evenly distributed on the surface of porous 3D graphene. Furthermore, we prepared an AuNPs-3D graphene interdigitated array electrode using the one-step laser induction method, which was used to fabricate a flexible impedimetric immunosensor for the detection of *Escherichia coli* O157:H7. The immunosensor shows excellent performance including low detection limit, high selectivity, and great flexibility.

1. Introduction

Three-dimensional (3D) graphene with porous structure possesses large surface area, good biocompatibility, and favorable electrical conductivity, which has been applied to various applications such as energy device (Cao et al., 2014; Xia et al., 2014; Xu et al., 2015), catalysis (Qiu et al., 2018), separation (Shen et al., 2015) and sensing (Li et al., 2015; Shu et al., 2018; Zeng et al., 2018). The 3D graphene can be prepared using various methods including self-assembly (Jiang et al., 2010; Xu et al., 2015), template-assisted preparation (Cao et al., 2011; Chen et al., 2011; Zhou et al., 2013), and direct deposition (Mao et al., 2013). Recently, a novel synthesized method (*i.e.* laser induction method) has been reported to synthesize 3D porous graphene from polyimide through directly scribing laser on the flexible polyimide membrane (Lin et al., 2014). The laser-induced graphene (LIG) can be patterned in any shapes with short time and large-scale production (Wang et al., 2018). Thus these advantages make it of high potential in the applications of microsupercapacitors (Li et al., 2017; Peng et al., 2015; Song et al., 2018), water splitting (Ye et al., 2017; Zhang et al., 2018b), antifouling (Singh et al., 2018), water treatment (Rathinam et al., 2017), and sensing (Cardoso et al., 2019; Garland et al., 2018; Tao et al., 2017).

Recently, hybrid materials by incorporation of active nanoparticles into the LIG with improved physical and chemical properties have been reported (Zang et al., 2018; Zhang et al., 2018a). Compared with LIG or active nanoparticles, the hybrid materials usually show improved performance due to the synergistic effect of LIG and nanoparticles. The LIG with 3D porous scaffolds leads to the high loading of nanoparticles to avoid the aggregation of nanoparticles in the application such as catalytic reaction. Meanwhile, the incorporation of active nanoparticles can introduce novel function or improve the performance (Luo and Zhi, 2015; Mao et al., 2015).

The hybrid materials can be prepared through various methods. For example, Tour's group successfully synthesized the metal oxide-LIG hybrid nanostructure using laser induction (Ye et al., 2015). The metal-complex-containing polyimide film was prepared by adding metal precursors into polyimide formulation. And then laser was applied to polyimide film containing metal precursors to form the metal oxide nanocrystals embedded in LIG. Various metal oxides such as Co_3O_4, MoO_2, and Fe_3O_4 can be grown on the surface of LIG in uniform and dense distribution, demonstrating the universality of this method for synthesizing metal oxide-LIG hybrid nanostructures. However, the preparation process of polyimide film containing metal precursors needs harsh condition such as high temperature, high pressure, and complex formulation. In addition, electrochemical deposition of metal

* Corresponding author.
E-mail address: yixianwang@zju.edu.cn (Y. Wang).

https://doi.org/10.1016/j.bios.2019.111896
Received 1 October 2019; Received in revised form 8 November 2019; Accepted 14 November 2019
Available online 20 November 2019

nanoparticles on the LIG is another typical method for the preparation of the metal-LIG hybrid nanocomposites (Dosi et al., 2019; Li et al., 2016; Yu et al., 2018). For example, Hu's group first patterned six-unit porous graphene interdigitated array electrodes using laser induction (Yu et al., 2018). The uniform and dense AuNPs were grown on the porous 3D graphene electrode surface through electrochemical deposition method for further application. One of the key limitations of this method is that need two steps to obtain the nanoparticles-LIG hybrid nanostructure, which is time-consuming and laborious. In addition, the attachment interaction of AuNPs on 3D graphene through electrochemical method is not strong, making the instability of sensor.

Herein, we proposed a novel one-step method for synthesizing metal nanoparticle-LIG hybrid nanostructures (Scheme 1). Chitosan-mediated ink containing metal precursor was first blade coating on the polyimide film. The as-prepared metal precursor modified polyimide film are then laser scanned to form porous metal nanoparticle-graphene nanocomposites. This method is quite general for the preparation of various metal nanoparticle-LIG, including AuNPs-LIG, AgNPs-LIG, and PtNPs-LIG. The prepared noble metal nanoparticles on LIG surface are uniform and dense. Furthermore, we used this method for patterning a flexible AuNPs-porous graphene electrode in interdigitated array configuration. The antibodies were modified on the surface of AuNPs-graphene interdigitated array electrode through physical adsorption between antibodies and AuNPs for constructing a flexible biosensor to detect *E. coli* O157:H7. The developed biosensor shows excellent performance including low detection limit, high selectivity, stability and flexibility.

2. Experimental

2.1. Materials and reagents

Chitosan was purchased from Aladdin (Shanghai, China). silver nitrate ($AgNO_3$), glacial acetic acid solution, gold(III) chloride trihydrate ($HAuCl_4{\cdot}3H_2O$), bovine serum albumin (BSA) and chloroplatinic acid hexahydrate (H_2PtCl_6) were purchased from Sinopharm (Shanghai, China). Silver paste and hydrophilic reagent were purchased from Prtronic (Shanghai, China). Polyimide film (thickness of 80 μm) were purchased from Dupont TM (USA). Phosphate-buffered saline (PBS) was obtained from BBI Life Sciences (Shanghai, China). Goat anti-*E. coli* O157:H7 antibody, *Listeria monocytogenes* (*L. monocytogenes*), *E. coli* O157:H7, *Staphylococcus aureus* (*S. aureus*), and *Vibrio parahaemolyticus* (*V. parahaemolyticus*) were purchased from Kirkegaard & perry Laboratories (KPL, Gaithersburg, MD).

2.2. Characterization

The scanning electron microscopy (SEM) images were obtained by Field emission scanning electron microscope (SU8010, Hitachi, Japan). Transmission electron microscopy (TEM) images were acquired from a Transmission electron microscope (JEM-1200EX, JEOL, Kyoto, Japan). High resolution TEM (HRTEM) characterization was carried out using a Field emission transmission electron microscope (Tecnai G^2 F20 S-TWIN, FEI, USA) equipped with an energy dispersive X-ray spectrometer (EDX). Raman spectroscopy measurements were carried out on a Lab-RAM HR Evolution Raman microscope system (Horiba Jobin Yvon, Piscataway, USA). X-ray photoelectron spectroscopy (XPS) measurements were evaluated by the AXIS Supra spectrometer (AXIS Supra, Kratos, UK).

2.3. Preparation of metal nanoparticle-LIG hybrid nanostructure using laser induction

Firstly, 40 mg of chitosan was dissolved in 5 mL glacial acetic acid solution (1.0%) and mixed by stirring for 2 h. Then, 2 mL of $HAuCl_4$ aqueous solution with different concentrations (25–100 mM), or 2 mL of $AgNO_3$ aqueous solution (150 mM), 2 mL of H_2PtCl_6 aqueous solution (75 mM) was mixed with 5 mL of as-prepared chitosan solution and the mixed solution was stirred for 1 h to obtain the metal precursor-chitosan hydrogel ink.

A hydrophilic solution was blade coating on polyimide film surface and dried in air at room temperature. Then gold precursor-chitosan hydrogel ink was further blade coating on the film and dried at 50 °C for 10 min using a hot plate. The polyimide film coating with hydrogel ink was patterned using a computer-controlled laser scribing micromachining system (Nano Pro-III, Jiayin, Tianjin, China) with different power varying from 2.20 to 3.85 W, and scan speed from 1 to 3 cm s^{-1}.

2.4. Fabrication of the AuNPs-LIG interdigitated array electrode

The AuNPs-LIG interdigitated array electrode was patterned by direct scribing laser on the gold precursor-chitosan hydrogel ink coated polyimide film. The width and gap of the interdigitated electrode were set to 250 μm and 400 μm, respectively. After that, silver paste was applied on both sides of the electrode for better electrical contact. Then, a Kapton polyimide tape was covered on the non-working area of the electrode to avoid contacting with electrolyte during the test.

2.5. Fabrication of an impedimetric immunosensor

Briefly, a droplet (0.5 mg mL^{-1}, 20 μL) of goat anti-*E coli* O157:H7 antibody was added on electrode surface and incubated overnight at 4 °C. After that, the electrode was washed using PBS buffer, and then dried with N_2. The electrode was then incubated with BSA blocking agent (1%, 20 μL) for 40 min at room temperature to avoid non-specific absorption, followed by washing with PBS buffer and dried with N_2. Finally,

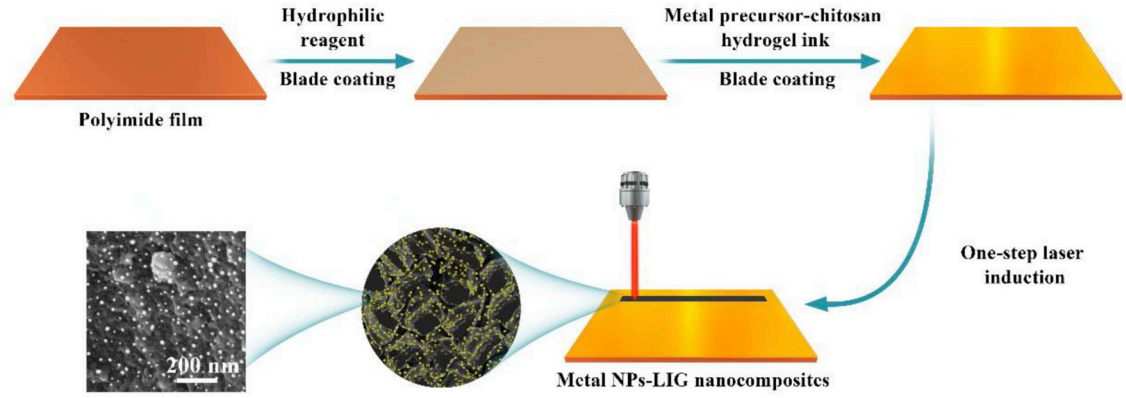

Scheme 1. Schematic illustration of the formation process of metal nanoparticle-LIG hybrid nanocomposites using one-step laser induction method.

different concentrations of *E coli* O157:H7 solutions (1×10^2–1×10^8 cfu mL^{-1}) were placed on the electrode surface and incubated for 30 min. The electrode was washed with PBS buffer and dried with N_2 for further impedance test.

2.6. Electrochemical measurements

The impedance test was carried on a Solartron analytical instrument (Solartron analytical 1260 and 1287, Farnborough, UK), and the experiment was supported by the Zview and Zplot software. The test electrolyte was 0.1 M KCl solution containing 5.0 mM $K_3Fe(CN)_6/K_4Fe(CN)_6$ (1:1). The alternating current voltage and frequency range was 10 mV and 0.1–100 kHz, respectively.

3. Results and discussion

The AuNPs-LIG hybrid nanocomposites were synthesized using a one-step laser induction method. First, the polyimide film was coated with a hydrophilic layer using blade coating method to improve the hydrophilicity of polyimide film. After that, gold precursor-chitosan hydrogel ink was further coated on the polyimide film for laser induction. The morphology and structure of the obtained AuNPs-LIG nanocomposites were characterized by SEM, TEM, EDX, HRTEM, Raman spectroscopy, and XPS. As shown in the SEM image (Fig. 1a), a porous 3D graphene form, which is similar to the previous literatures (Li et al., 2016; Yu et al., 2018). According to the high magnification SEM image (Fig. 1b), the AuNPs are decorated on the 3D graphene surface in uniform and dense distribution. Fig. 1c shows the TEM image of a typical AuNPs-LIG nanocomposite, exhibiting sheet like structure. According to data statistics in Fig. 1d, the corresponding average diameters of AuNPs on the surface of graphene is ~10.1 nm (Fig. 1e). The AuNPs-LIG nanocomposite displays clear lattice fringes in the HRTEM (Fig. 1f). The lattice spacing is 0.24 nm, assignable to (111) plane of Au. The EDX elemental mapping of the nanocomposites in Fig. S1 shows that there are Au, C, N, and O elements evenly distributed on the nanosheets, confirming the growth of AuNPs on the graphene surface. Raman spectra of the nanocomposites displays that there are two peaks at 2700 and 1585 cm^{-1} (Fig. 1g), originated at 2D and G peaks of graphene (Cai et al., 2018). As shown in the XPS data of AuNPs-LIG (Fig. 1h), the presence of two peaks at 87.5 and 83.8 eV in the Au 4f XPS spectrum demonstrates that only metallic state of Au existed in AuNPs-LIG nanocomposites (Qiu et al., 2019).

Several synthesis parameters, including laser power, scan rate, and gold precursor concentrations, on the influence of the morphology and structure of the prepared AuNPs-LIG nanocomposites were studied. The SEM images of AuNPs-LIG nanocomposites obtained by various laser power of 2.2, 2.75, 3.30 and 3.85 W at a scan rate of 2.0 cm s^{-1} and a $HAuCl_4$ concentration of 50 mM are shown in Fig. S2, the size of AuNPs become larger as the laser intensity increases. The AuNPs-LIG nanocomposites were prepared by various scan rate of 3.0, 2.0 and 1.0 cm s^{-1} at a laser power of 3.3 W and $HAuCl_4$ concentration of 50 mM. In these SEM images (Fig. S3), the size of AuNPs becomes larger as the scanning rate decreases. According to the above results, higher laser power and lower scan rate will result in larger particles of AuNPs. According to the Raman spectra of the prepared materials using different scan rate (Fig. S4a) and laser power (Fig. S4b), there are two peaks of ~2700 and 1585 cm^{-1} corresponding to the 2D and G peaks of graphene, indicating the intrinsic property of graphene in the prepared AuNPs-LIG. Furthermore, we also explored the effect of the concentrations of $HAuCl_4$ on the growth of AuNPs on surface of 3D graphene. As shown in Fig. S5, as the concentration of $HAuCl_4$ increases from 25 mM to 100 mM, the number of the grown AuNPs increases and the size of AuNPs becomes larger. The TEM images of AuNPs-LIG nanocomposites produced by various $HAuCl_4$ concentrations are shown in Figs. S6a–d. The particles are evenly distributed on the surface of graphene. According to the data statistics of AuNPs in TEM images (Figs. S6e–h), the size of AuNPs on the surface of 3D graphene is ~4.3, 10.1, 12.8, and 14.3 nm, when the AuNPs-LIG nanocomposites were prepared using different concentrations of $HAuCl_4$ (25, 50, 75, and 100 mM), respectively.

To demonstrate the universality of our proposed method, another two kinds of metal nanoparticle-LIG nanocomposites including AgNPs-LIG and PtNPs-LIG nanocomposites were also synthesized. Fig. 2a shows the SEM image of AgNPs-LIG nanocomposites, in which a porous 3D graphene is formed. After amplification of the SEM image (Fig. 2b), the uniform AgNPs evenly distributed on the surface of porous 3D graphene can be observed. Fig. 2c shows a TEM image of AgNPs-LIG nanocomposite. The low contrast of the prepared material indicates the layered-structure of graphene in AgNPs-LIG nanocomposite. According to the statistics with the TEM image of AgNPs-LIG nanocomposite (Fig. 2d), the average diameter of the AgNPs is about 9.6 nm (Fig. 2e). The lattice fringe in the HRTEM image is 0.25 nm (Fig. 2f),

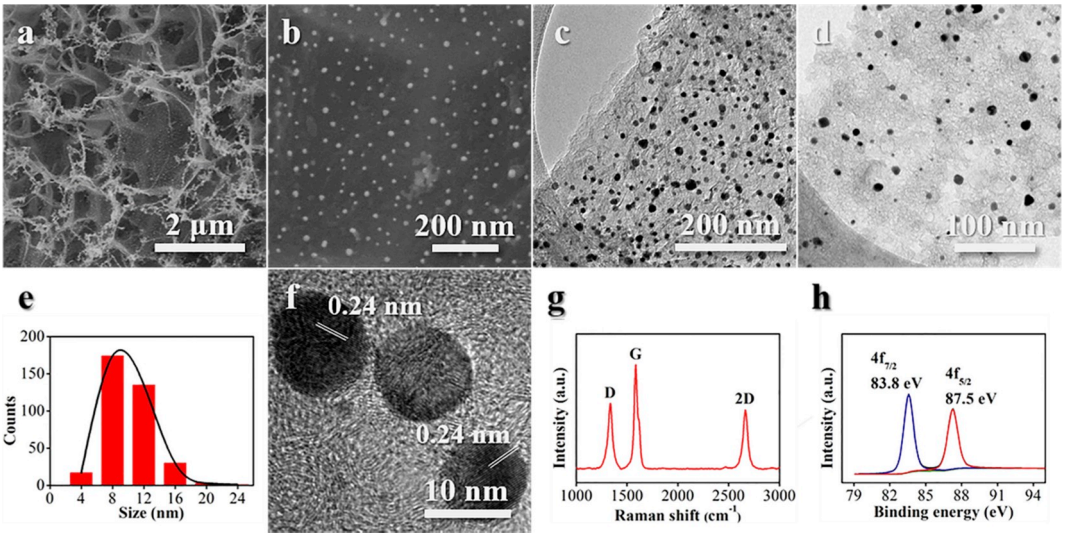

Fig. 1. Characterization for the morphology and chemical composition of the AuNPs-LIG nanocomposite prepared using one-step laser induction. (a) SEM image of the AuNPs-LIG nanocomposite; (b) Higher magnification SEM image of the AuNPs-LIG nanocomposite; (c) TEM image of a typical AuNPs-LIG nanocomposite; (d) Higher magnification TEM image of AuNPs-LIG nanocomposite; (e) Statistics of the size of AuNPs distributed on the surface of porous 3D graphene; (f) HRTEM image showing crystalline AuNPs on LIG; (g) Raman spectra of the AuNPs-LIG nanocomposite; (h) XPS spectra of the AuNPs-LIG nanocomposite.

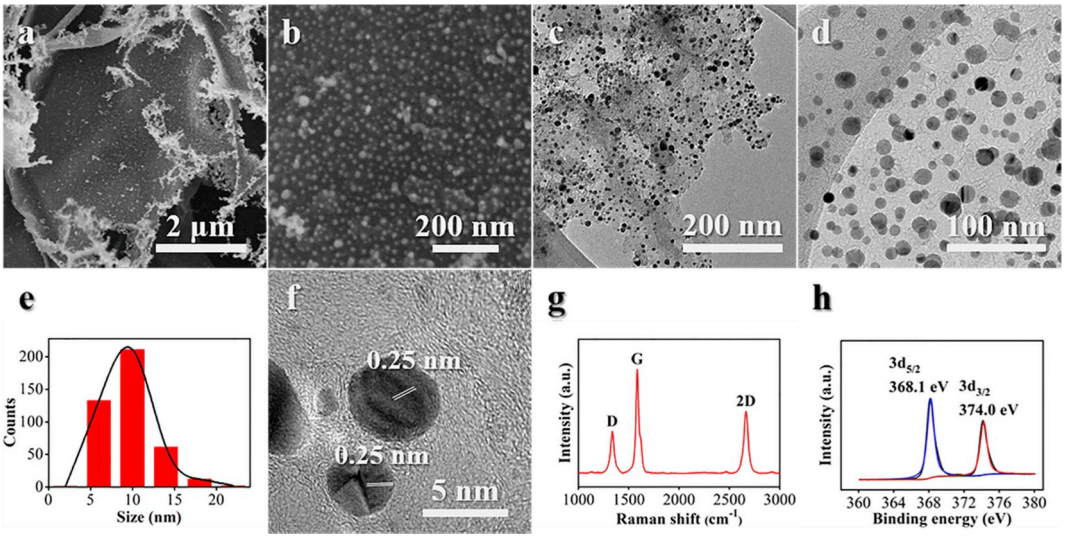

Fig. 2. Characterization for the morphology and chemical composition of the AgNPs-LIG nanocomposite prepared using one-step laser induction. (a) SEM image of the AgNPs-LIG nanocomposite; (b) Higher magnification SEM image of the AgNPs-LIG nanocomposite; (c) TEM image of a typical AgNPs-LIG nanocomposite; (d) Higher magnification TEM image of AgNPs-LIG nanocomposite; (e) Statistics of the size of AgNPs distributed on the surface of porous 3D graphene; (f) HRTEM image showing crystalline AgNPs on LIG; (g) Raman spectra of the AgNPs-LIG nanocomposite; (h) XPS spectra of the AgNPs-LIG nanocomposite.

assignable to 1/3(422) plane of AgNPs. The EDX elemental mapping of the nanocomposites in Fig. S7 shows that there are Ag, C, N, O elements, further proving the uniform presence of AgNPs on the surface of graphene. Two peaks at ~2700 and 1585 cm^{-1} are exhibited in the Raman spectra (Fig. 2g), which corresponds to the 2D and G peaks of graphene. As shown in the XPS result of AgNPs-LIG nanocomposites (Fig. 2h), there are two peaks at 368.1 and 374.0 eV corresponding to Ag $3d_{5/2}$ and Ag $3d_{3/2}$, indicating that only metallic state of Ag existed in nanocomposite (Qiu et al., 2019). The prepared PtNPs-LIG nanocomposites were characterized by SEM, TEM, Raman spectra, and XPS. According to the SEM images (Fig. 3a and b), we can see that the Pt NPs were evenly decorated on the surface of porous 3D graphene. A typical PtNPs-LIG nanosheet was shown in the TEM image (Fig. 3c). Furthermore, the average diameter of the PtNPs is ~7.6 nm (Fig. 3d and e). As shown in the high-resolution TEM image, the lattice fringe is 0.22 nm (Fig. 3f), assignable to (111) plane of PtNPs. The EDX images show that Pt, C, N and O elements are evenly distributed on the nanosheet (Fig. S8), which indicates the successful preparation of the PtNPs-LIG nanocomposite. Raman spectra shows there are two peaks at ~2700 and 1585 cm^{-1} corresponding to the 2D and G peaks of graphene (Fig. 3g), demonstrating the formation of 3D graphene through laser induction. As shown in XPS curve of AgNPs-LIG nanocomposite (Fig. 3h), the peaks at about 71.3 and 74.6 eV could be originated from Pt $4f_{7/2}$ and Pt $4f_{5/2}$, indicating that only metallic state of Pt existed in nanocomposite (Chen et al., 2018).

The flexible biosensor with lightweight and ultrathin properties as well as high sensing performance is urgently needed in the field of sensing applications in vivo and vitro (Chen and Pei, 2017; Han et al., 2017; Liu et al., 2017; Singh et al., 2017; Zhao et al., 2017). The metal nanoparticle-LIG nanocomposites prepared using our proposed method possess several advantages including large surface area, good biocompatibility, and high conductivity. In addition, the nanocomposites can be

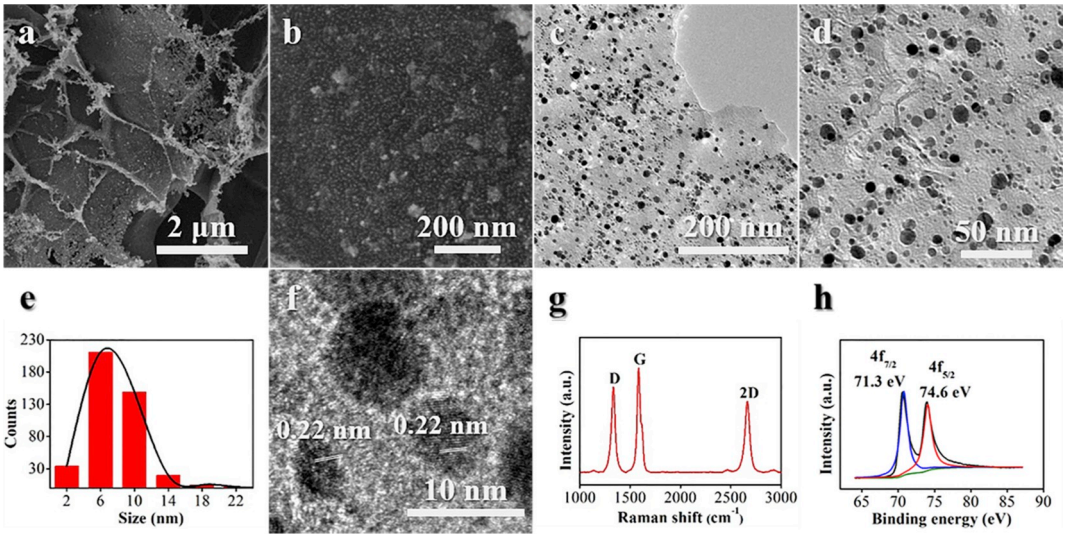

Fig. 3. Characterization for the morphology and chemical composition of the PtNPs-LIG nanocomposite prepared using one-step laser induction. (a) SEM image of the PtNPs-LIG nanocomposite; (b) Higher magnification SEM image of the PtNPs-LIG nanocomposite; (c) TEM image of a typical PtNPs-LIG nanocomposite; (d) Higher magnification TEM image of PtNPs-LIG nanocomposite; (e) Statistics of the size of PtNPs distributed on the surface of porous 3D graphene; (f) HRTEM image showing crystalline PtNPs on LIG; (g) Raman spectra of the PtNPs-LIG nanocomposite; (h) XPS spectra of the PtNPs-LIG nanocomposite.

patterned into various shapes and the substrate (polyimide film) is flexible, which is suitable for developing flexible biosensing devices. Therefore, we prepared an AuNPs-LIG interdigitated array electrode using the one-step laser induction method, which was used to fabricate an immunosensor for detecting foodborne pathogen. Fig. 4a shows the fabrication process of the flexible interdigitated array electrode. The AuNPs-LIG interdigitated array electrode was patterned by direct scribing laser on the gold precursor-chitosan hydrogel ink coating polyimide film (Fig. S9). As shown in Fig. S10, the width and gap of the interdigitated electrode were about 250 μm and 400 μm, respectively. After that, silver paste was applied on both sides of the electrode for better electrical contact. Then, a Kapton polyimide tape was covered on the non-working area of the electrode to avoid contacting with electrolyte (Fig. 4c).

The whole fabrication process of the AuNPs-LIG electrode-based immunosensor includes antibody modification, BSA blocking, and pathogen capture (Fig. 4b). Fig. 4d shows the Nyquist plots of these assembly steps for investigating the interfacial properties. The electron transfer resistance (R_{et}) representing the semicircle diameter of the AuNPs-LIG interdigitated array electrode is quite small due to the good conductivity of AuNPs-LIG, contributing to high electron transfer (Kong et al., 2016). The R_{et} of AuNPs-LIG electrode decreases when the AuNPs grows on the surface of LIG electrode (Fig. S11), which further indicates that the AuNPs-LIG nanocomposites have the potential to improve the sensitivity of immunosensor. When the antibody and BSA was immobilized on the electrode surface, the R_{et} increases in succession. This is because that antibody and BSA are all biomacromolecules, which can adsorb on the surface of AuNPs through physical adsorption. The adsorbed antibody and BSA would produce kinetics barrier for redox probe, resulting in the enhancement of the corresponding R_{et}. After capture of *E. coli* O157:H7, the R_{et} further increases. According to the previous report (Wang et al., 2013), the membrane of bacteria shows a resistance of 10^2–10^5 Ω cm^2, which hinders the redox probe transfer on the electrode surface. The results proved the feasibility of the AuNPs-LIG interdigitated array electrode-based impedimetric sensor for detecting *E. coli* O157:H7. For control experiments, we used equal amount of pure PBS to replace antibodies solution in the process of antibody modification and measured the impedance of the electrodes. In BSA blocking and bacteria capture, similar procedures were conducted by replacing the corresponding agents with pure PBS. Comparing the values of R_{et} between the experimental group and control group (as shown in Fig. S12 and Table S1), it could be clearly seen that the impedance change in each step was due to the antibody modification, BSA blocking, and bacteria capture. The typical Randles equivalent circuit which includes a solution resistance (R_s), a double layer capacitance (C_{dl}) in parallel with a R_{et} and a Warburg resistance (Z_W) was used for fitting the tested impedance spectra. As shown in Fig. 4e, the equivalent circuit can be well fitting the impedance spectra. The fitting value of AuNPs-LIG electrode, antibody immobilization, BSA blocking and bacteria capture were listed in Table S1, in which the R_{et} shows the largest change after each step. Therefore, R_{et} was applied to analyze the impedance change in the following experiments.

Different concentrations of pathogens were incubated with the antibody modified AuNPs-LIG interdigitated array electrode and the corresponding Nyquist plots were recorded. As shown in Fig. 5a, when the *E. coli* O157:H7 with different concentrations at range from 1×10^2 cfu mL^{-1} to 1×10^8 cfu mL^{-1} were incubated with the electrode, the semicircle diameters of impedance spectra increase. The corresponding R_{et} exhibits a good linearity with the concentrations of *E. coli* O157:H7 (1×10^2–1×10^8 cfu mL^{-1}) and the detection limit is estimated to be 1×10^2 cfu mL^{-1} (Fig. 5b).

The specificity is one of the key parameters to evaluate the performance of the developed immunosensor. Thus we used several non-target microorganisms including *S. aureus*, *V. parahaemolyticus* and *L. monocytogenes* to investigate the specificity of the developed impedimetric biosensor. Compared with that of *E. coli* O157:H7, no significant impedance response was found for these non-target bacteria, demonstrating the high specificity of the developed impedimetric biosensor (Fig. 5c). Another key parameter, flexibility of the proposed biosensor, was also investigated. As shown in Fig. S13, our

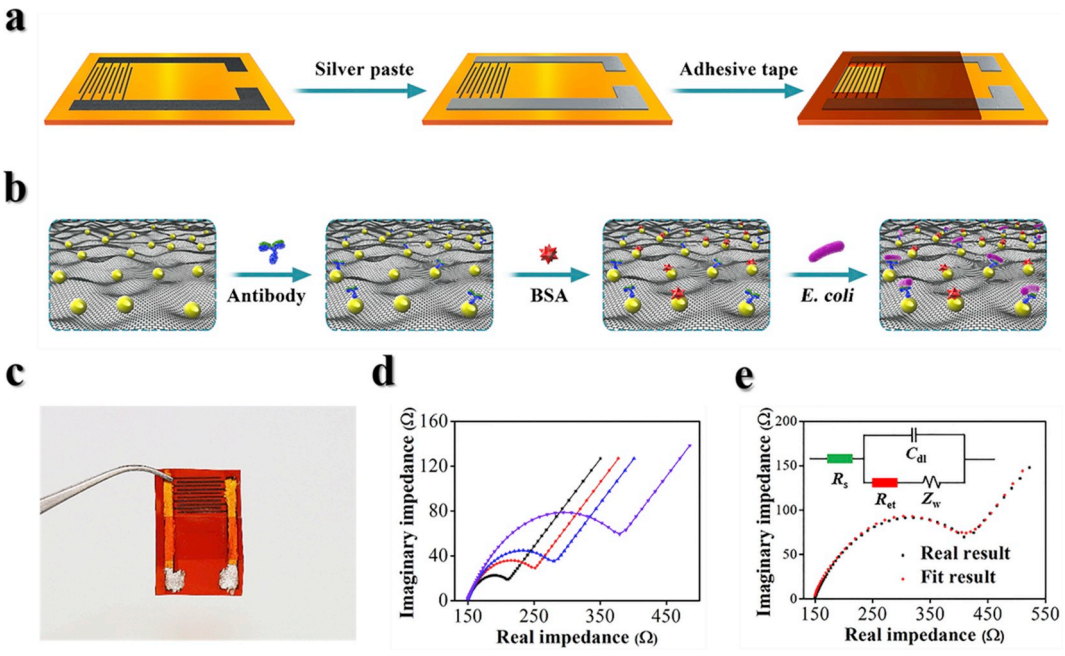

Fig. 4. (a) Schematic illustration of the fabrication process of the AuNPs-LIG interdigitated array electrode using one-step laser induction; (b) Schematic illustration of the AuNPs-LIG interdigitated array electrode-based immunosensor for the detection of *E. coli* O157:H7; (c) Optical image of the prepared the AuNPs-LIG interdigitated array electrode; (d) Nyquist plots obtained with AuNPs-LIG electrode (black line), antibody modification (red line), BSA blocking (blue line), and bacteria capture (purple line); (e) The fitting curve of the impedance spectra using Randles equivalent circuit. The concentration of *E. coli* O157:H7 is 1×10^6 cfu mL^{-1} and the test solution is 0.1 M KCl solution containing 5 mM $[Fe(CN)_6]^{3-/4-}$. (For interpretation of the references to colour in this figure legend, the reader is referred to the Web version of this article.)

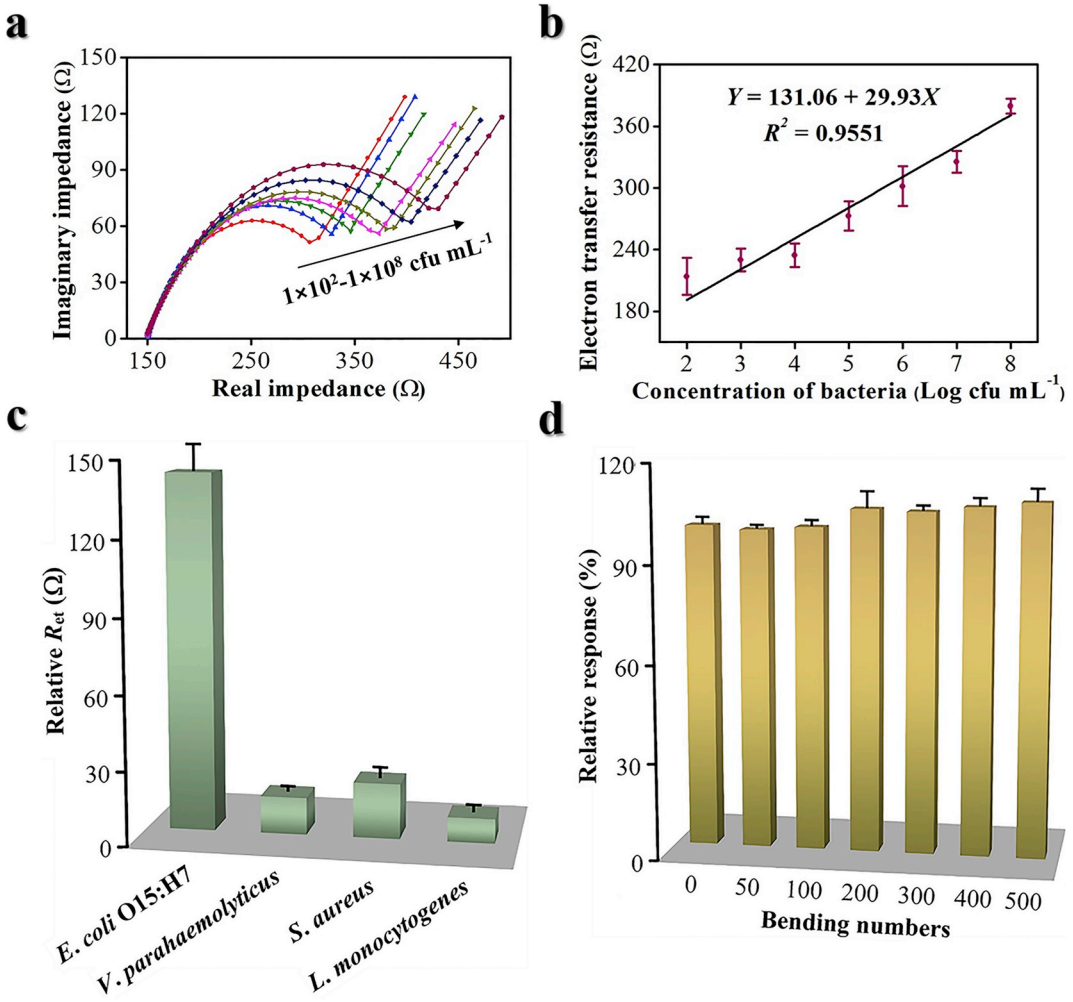

Fig. 5. (a) Nyquist plots and (b) calibration curve of the impedance response and the concentrations of *E. coli* O157:H7 (1×10^2–1×10^8 cfu mL^{-1}); (c) Specificity of the AuNPs-LIG interdigitated array electrode-based impedimetric immunosensor; (d) Flexibility test of the AuNPs-LIG interdigitated array electrode-based impedimetric immunosensor.

immunosensor possesses great flexibility. The bending effect on the impedance response of the biosensor to *E. coli* O157:H7 was tested (Fig. 5d). The change of the impedance response of the immunosensor is less than 10% after bending the electrode for 500 times, indicating the excellent flexibility of the fabricated immunosensor.

4. Conclusions

In summary, we developed a one-step laser induction method for preparing various metal nanoparticle-LIG nanocomposites (AuNPs-LIG, AgNPs-LIG, and PtNPs-LIG). The synthesized parameters including laser power, scan speed, and metal precursor concentration were investigated. The prepared AuNPs-LIG interdigitated array electrode using the one-step laser induction method shows high conductivity, large surface area, good biocompatibility, and great flexibility. Based on this, a flexible impedimetric immunosensor using the AuNPs-LIG interdigitated array electrode for the detection of *E. coli* O157:H7 was developed. The developed immunosensor exhibits excellent performance including low detection limit, high selectivity, and great flexibility, which holds great potential in the routine sensing applications.

Declaration of competing interest

The authors declare that they have no known competing financial interests or personal relationships that could have appeared to influence the work reported in this paper.

CRediT authorship contribution statement

Zhiheng You: Conceptualization, Data curation, Formal analysis, Writing - original draft. **Qiming Qiu:** Investigation. **Huayun Chen:** Methodology. **Yuyan Feng:** Software. **Xiao Wang:** Validation. **Yixian Wang:** Project administration, Writing - review & editing, Supervision. **Yibin Ying:** Writing - review & editing.

Acknowledgements

The authors are grateful for the financial support from National Natural Science Foundation of China (No. 31571922).

Appendix A. Supplementary data

Supplementary data to this article can be found online at https://doi.org/10.1016/j.bios.2019.111896.

References

Cai, G., Yu, Z., Ren, R., Tang, D., 2018. ACS Sens. 3 (3), 632–639.
Cao, X., Shi, Y., Shi, W., Lu, G., Huang, X., Yan, Q., Zhang, Q., Zhang, H., 2011. Small 7 (22), 3163–3168.
Cao, X., Yin, Z., Zhang, H., 2014. Energy Environ. Sci. 7 (6), 1850–1865.

Cardoso, A.R., Marques, A.C., Santos, L., Carvalho, A.F., Costa, F.M., Martins, R., Sales, M.G.F., Fortunato, E., 2019. Biosens. Bioelectron. 124, 167–175.
Chen, D., Pei, Q.B., 2017. Chem. Rev. 117 (17), 11239–11268.
Chen, H.Y., Qiu, Q.M., Sharif, S., Ying, S.N., Wang, Y.X., Ying, Y.B., 2018. ACS Appl. Mater. Interfaces 10 (28), 24108–24115.
Chen, Z., Ren, W., Gao, L., Liu, B., Pei, S., Cheng, H.-M., 2011. Nat. Mater. 10 (6), 424–428.
Dosi, M., Lau, I., Zhuang, Y., Simakov, D.S.A., Fowler, M.W., Pope, M.A., 2019. ACS Appl. Mater. Interfaces 11 (6), 6166–6173.
Garland, N.T., McLamore, E.S., Cavallaro, N.D., Mendivelso-Perez, D., Smith, E.A., Jing, D., Claussen, J.C., 2018. ACS Appl. Mater. Interfaces 10 (45), 39124–39133.
Han, S.T., Peng, H.Y., Sun, Q.J., Venkatesh, S., Chung, K.S., Lau, S.C., Zhou, Y., Roy, V.A. L., 2017. Adv. Mater. 29 (33), 1700375.
Jiang, X., Ma, Y., Li, J., Fan, Q., Huang, W., 2010. J. Phys. Chem. C 114 (51), 22462–22465.
Kong, D., Bi, S., Wang, Z., Xia, J., Zhang, F., 2016. Anal. Chem. 88 (21), 10667–10674.
Li, L., He, S., Liu, M., Zhang, C., Chen, W., 2015. Anal. Chem. 87 (3), 1638–1645.
Li, L., Zhang, J., Peng, Z., Li, Y., Gao, C., Ji, Y., Ye, R., Kim, N.D., Zhong, Q., Yang, Y., Fei, H., Ruan, G., Tour, J.M., 2016. Adv. Mater. 28 (5), 838–845.
Li, Y., Luong, D.X., Zhang, J., Tarkunde, Y.R., Kittrell, C., Sargunaraj, F., Ji, Y., Arnusch, C.J., Tour, J.M., 2017. Adv. Mater. 29 (27), 1700496.
Lin, J., Peng, Z., Liu, Y., Ruiz-Zepeda, F., Ye, R., Samuel, E.L.G., Yacaman, M.J., Yakobson, B.I., Tour, J.M., 2014. Nat. Commun. 5, 5714.
Liu, Y.Q., He, K., Chen, G., Leow, W.R., Chen, X.D., 2017. Chem. Rev. 117 (20), 12893–12941.
Luo, B., Zhi, L., 2015. Energy Environ. Sci. 8 (2), 456–477.
Mao, S., Lu, G., Chen, J., 2015. Nanoscale 7 (16), 6924–6943.
Mao, S., Yu, K., Chang, J., Steeber, D.A., Ocola, L.E., Chen, J., 2013. Sci. Rep. 3, 1696.
Peng, Z., Ye, R., Mann, J.A., Zakhidov, D., Li, Y., Smalley, P.R., Lin, J., Tour, J.M., 2015. ACS Nano 9 (6), 5868–5875.
Qiu, B., Xing, M., Zhang, J., 2018. Chem. Soc. Rev. 47 (6), 2165–2216.
Qiu, Q.M., Chen, H.Y., Sharif, S., You, Z.H., Ying, S.N., Wang, Y.X., Ying, Y.B., 2019. 2D Mater. 6 (3), 035008.
Rathinam, K., Singh, S.P., Li, Y., Kasher, R., Tour, J.M., Arnusch, C.J., 2017. Carbon 124, 515–524.
Shen, Y., Fang, Q., Chen, B., 2015. Environ. Sci. Technol. 49 (1), 67–84.
Shu, J., Qiu, Z., Tang, D., 2018. Anal. Chem. 90 (16), 9691–9694.
Singh, E., Meyyappan, M., Nalwa, H.S., 2017. ACS Appl. Mater. Interfaces 9 (40), 34544–34586.
Singh, S.P., Li, Y., Zhang, J., Tour, J.M., Arnusch, C.J., 2018. ACS Nano 12 (1), 289–297.
Song, W., Zhu, J., Gan, B., Zhao, S., Wang, H., Li, C., Wang, J., 2018. Small 14 (1), 1702249.
Tao, L.-Q., Tian, H., Liu, Y., Ju, Z.-Y., Pang, Y., Chen, Y.-Q., Wang, D.-Y., Tian, X.-G., Yan, J.-C., Deng, N.-Q., Yang, Y., Ren, T.-L., 2017. Nat. Commun. 8, 14579.
Wang, Y., Wang, Y., Zhang, P., Liu, F., Luo, S., 2018. Small 14 (36), 1802350.
Wang, Y.X., Ping, J.F., Ye, Z.Z., Wu, J., Ying, Y.B., 2013. Biosens. Bioelectron. 49, 492–498.
Xia, X.H., Chao, D.L., Zhang, Y.Q., Shen, Z.X., Fan, H.J., 2014. Nano Today 9 (6), 785–807.
Xu, Y., Shi, G., Duan, X., 2015. Acc. Chem. Res. 48 (6), 1666–1675.
Ye, R., Chyan, Y., Zhang, J., Li, Y., Han, X., Kittrell, C., Tour, J.M., 2017. Adv. Mater. 29 (37), 1702211.
Ye, R., Peng, Z., Wang, T., Xu, Y., Zhang, J., Li, Y., Nilewski, L.G., Lin, J., Tour, J.M., 2015. ACS Nano 9 (9), 9244–9251.
Yu, Y., Joshi, P.C., Wu, J., Hu, A., 2018. ACS Appl. Mater. Interfaces 10 (40), 34005–34012.
Zang, X., Shen, C., Chu, Y., Li, B., Wei, M., Zhong, J., Sanghadasa, M., Lin, L., 2018. Adv. Mater. 30 (26), 1800062.
Zeng, R., Luo, Z., Zhang, L., Tang, D., 2018. Anal. Chem. 90, 12299–12306.
Zhang, J., Ren, M., Li, Y., Tour, J.M., 2018. ACS Energy Lett. 3 (3), 677–683.
Zhang, J., Ren, M., Wang, L., Li, Y., Yakobson, B.I., Tour, J.M., 2018. Adv. Mater. 30 (21), 1707319.
Zhao, S.F., Li, J.H., Cao, D.X., Zhang, G.P., Li, J., Li, K., Yang, Y., Wang, W., Jin, Y.F., Sun, R., Wong, C.P., 2017. ACS Appl. Mater. Interfaces 9 (14), 12147–12164.
Zhou, M., Lin, T., Huang, F., Zhong, Y., Wang, Z., Tang, Y., Bi, H., Wan, D., Lin, J., 2013. Adv. Funct. Mater. 23 (18), 2263–2269.